

<https://doi.org/10.1038/s43247-025-02088-5>

Mackinawite partial oxidation to green rust produces a large, abiotic uranium isotope fractionation

Check for updates

Romain Guilbaud¹ ✉, Morten B. Andersen², Helen M. Freeman³, Jeffrey Paulo H. Perez⁴, David Uhlig⁵ & Liane G. Benning^{4,6}

Low-oxygen settings and transition zones between strictly anoxic and oxic conditions may have characterised large expanses of Precambrian continental margins, where oxygen-breathing, complex life emerged and diversified. Accurate reconstructions of oxygen levels in such conditions are therefore required, but current geochemical proxies fail in identifying transitional redox conditions. Uranium isotopes are an emerging palaeoredox proxy, as large isotope fractionations are recorded during the reduction of uranium into anoxic sediments. Their potential application to transitional conditions is, however, unclear, because the redox regulating mineralogy of such environments and the associated isotope fractionations are poorly constrained. Here, we explore the mineralogical transformations occurring during the partial oxidation of mackinawite. We show that green rust, a key mineral of Precambrian oceans, forms as a by-product of mackinawite oxidation, along with uraninite and polysulphide. We also demonstrate that this mechanism records a large abiotic uranium isotope fractionation during its reaction with aqueous iron sulphide.

The isotopic variability of uranium (U) isotopes is being increasingly used on ancient sedimentary rocks to reconstruct palaeoredox conditions^{1–6} in Proterozoic (2.5 to ~0.54 billion years ago, Ga) oceans. Their use has been applied predominantly to carbonates and black shales. In the first instance, this is due to limited U isotope fractionation during U incorporation into carbonates, which may, in some instances, record the seawater isotopic composition with limited diagenetic alterations^{2,7,8}. In the case of black shales, U isotopes fractionate (by up to ~1.2‰) during U reduction and fixation into anoxic sediments^{1,3,9,10}. However, Precambrian oceans were characterised by a range of oxygen-depleted conditions, from low-oxygen ('suboxic', here referred to as <100 μM [O₂]) levels to ferruginous (anoxic, ferrous iron-containing and non-sulphidic) conditions, and to euxinic (anoxic and sulphide-containing) conditions. All these conditions likely fractionate U isotopes in different ways. Hence, interpreting variations in sedimentary U isotope compositions requires a detailed understanding of the redox context in which U isotopes were transported and archived into anoxic sediments.

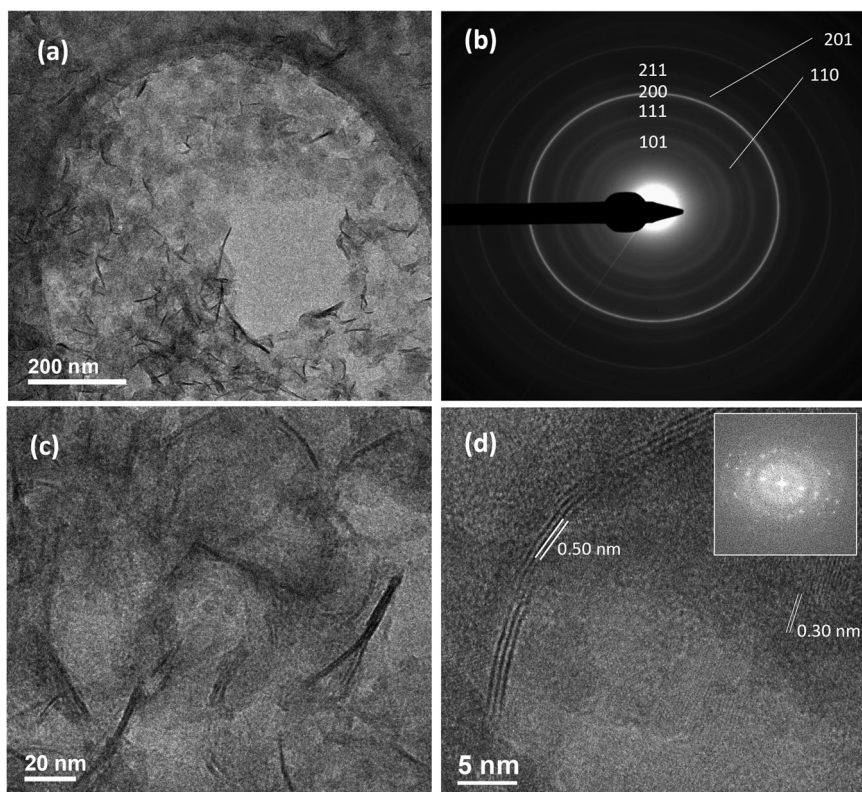
Throughout most of the Proterozoic, oceans were dominantly ferruginous^{11,12}, with oxic shallow waters and euxinic conditions spanning along productive continental margins^{12,13}. From ~1 Ga, the spread of euxinic

margins became severely limited^{14,15}, with expansive ferruginous conditions until the late Proterozoic^{16,17}. Dynamic fluctuations between oxic and ferruginous water masses^{18,19} eventually led to the establishment of modern-like oxygen minimum zones at the Proterozoic-Cambrian transition, with punctual euxinic conditions in basins with high organic influxes^{20–22}. This long-term evolution of ocean redox chemistry suggests that the application of the U isotope proxy to Precambrian sedimentary rocks demands enhanced knowledge on how U isotopes may fractionate in these distinct redox contexts.

Under ferruginous conditions, the formation of iron minerals such as ferrihydrite²³ and green rust²⁴ (a mixed Fe(II)/Fe(III) hydroxide, naturally occurring as either Fe₆(OH)₁₂SO₄ or Fe₆(OH)₁₂CO₃) in the water column may fractionate U isotopes through co-precipitation or adsorption processes, although the data is limited to few experimental studies^{25,26}. It has been suggested that U reduction by mixed Fe(II)/Fe(III) minerals such as magnetite and green rust lead to the reduced U(IV) products being isotopically light²⁶. This is contrasting with other field and experimental observations^{27,28}, which indicate that U(IV) phases incorporate preferentially heavy U isotopes, as is the case for mass independent isotope fractionation effects such as nuclear field shift fractionation. Unfortunately,

¹Centre National de la Recherche Scientifique (CNRS), Géosciences Environnement Toulouse (UMR 5563), 31400 Toulouse, France. ²School of Earth and Environmental Sciences, Cardiff University, Cardiff, CF10 3AT, UK. ³Priestley Centre for Climate Futures, University of Leeds, Leeds, LS2 9JT, UK. ⁴GFZ Helmholtz Centre for Geosciences, Telegrafenberg, 14473 Potsdam, Germany. ⁵Institut für Geologische Wissenschaften, Freie Universität Berlin, 12249 Berlin, Germany. ⁶Department of Earth Sciences, Freie Universität Berlin, 12249 Berlin, Germany. ✉e-mail: romain.guilbaud@cnrs.fr

Fig. 1 | Characterization of initial non-U reacted FeS. **a** TEM image of FeS sheet aggregates. **b** SAED patterns of (a) with peaks at 1.72 Å (201), 1.57 Å (211), 1.85 Å, 2.31 Å (111), 2.62 Å (110) and 3.03 Å (101), confirming that the particles only consist of mackinawite⁴⁷. **c, d** High resolution image and FFT showing *d*-spacing at 0.5 and 0.3 nm, supportive of nanoparticulate mackinawite⁴⁷.



natural observations in modern ferruginous analogues, which could potentially corroborate these experimental data, show a high variability in the U isotope compositions, presumably due to a range of isotope fractionation effects occurring during various biogeochemical pathways²⁹. Under euxinic conditions, U reduction is accompanied by a large isotope fractionation, which favours the incorporation of isotopically heavy U into the reduced phase and the sediments^{3,27}. In these euxinic settings, U reduction and removal are likely biologically mediated by, for example, sulphate-reducing bacteria³⁰. Mackinawite (here nominally labelled as FeS) occurs as the preponderant nanoparticulate Fe mineral within euxinic water columns, as its precipitation is kinetically favoured over pyrite (FeS₂)^{31–33}. While abiotic reduction of U(VI) to U(IV) on FeS surfaces is well known^{34,35}, contradictory experimental datasets suggest equivocal effects on the associated U isotope fractionations^{26,36}. In particular, the roles of adsorption versus reduction on the overall isotope fractionation have been notoriously difficult to distinguish in experimental set-ups³⁶.

In addition, dynamic shifts from euxinic to ferruginous or oxic conditions during the Precambrian may have resulted in the establishment of transient redox transitional zones. Despite the significance of such redox transitional zones for the Precambrian biota on continental margins, they have received relatively little attention. The study of such transitions in modern analogues (e.g., Arvadi Spring, Switzerland) suggests that in ferruginous-to-oxic and euxinic-to-oxic transition zones, the mineralogy of Fe- and S-bearing phases is dominated by green rust and elemental S, respectively³⁷. The formation of elemental S during the oxidation of FeS has also been documented experimentally^{34,35,38}. In these experiments, reported Fe-bearing products include either greigite (Fe₃S₄) as an intermediate phase during pyrite formation^{33,39}, or a range of iron oxide assemblages, such as hematite and magnetite⁴⁰, goethite and lepidocrocite⁴¹, and amorphous Fe(OH)₃ [refs. 42,43]. While ‘green rust-like’ precipitates have also been suggested to form under acidic pH during oxidation by selenate⁴¹ and chromate⁴⁴, green rust has never been reported as a Fe-bearing product of an FeS oxidation reaction by uranium at seawater pH.

Here, we explore experimentally the mechanism of FeS oxidation by U(VI) at seawater pH. Using high resolution transmission electron

microscopy (TEM) imaging and analyses, we report the end-product mineralogy for both Fe and U phases, and we track the evolution of U isotope compositions in both the dissolved and the solid phases. Ultimately, we provide a new key insight to interpret U isotope signatures in ancient anoxic transition zones, revisiting earlier views on abiotic U isotope fractionations.

Results

Characterization of initial conditions

Mackinawite precipitated by mixing of equimolar Fe(II) and S(-II) solutions, following previously published protocols⁴⁵. Immediately after mixing, well-developed nanoparticles with Fe-S composition and typical plate-structured aggregates^{46,47} formed (Fig. 1). This phase was identified as mackinawite through selected area diffraction (SAED, Fig. 1b) and fast Fourier transforms (FFT, Fig. 1d), and through the Fe/S ratios from cross-correlated X-ray photoelectron spectroscopic analyses (XPS, Fig. 2, Tables S1–S4).

This freshly precipitated FeS slurry was aged in its supernatant for one hour in order to allow for particle aggregation and equilibration⁴⁸. In a second step, a U(VI) solution (NaHCO₃-buffered at pH 8) was injected into this 1 h aged FeS slurry, and the mixture was further aged for various experimental durations (up to 1.17 h; Table 1). At set time points the resulting solids were separated from the supernatants through filtration (see the Supplementary methods 1 for full details on the protocols) and each component characterized. For longer-term experiments (up to 144 h), the uranium solution was added directly after FeS precipitation with no additional aging. Due to the bicarbonate buffer, dissolved U(VI) was largely dominated by the uranyl carbonate complex UO₂(CO₃)₂²⁻, as confirmed by aqueous speciation calculations (Figs. S1 and S2). The experimental setup was therefore comparable to previous studies^{26,36}, with a major difference being the higher pH (pH 8 compared to pH 6.8 and pH 7.1 in refs. 26,36, respectively). This higher pH was chosen to minimize the adsorption of negatively charged uranyl carbonate species onto mackinawite surfaces, which become positively charged at pH < 7.5 [ref. 49], inducing additional U isotope fractionations⁵⁰. However, whilst this efficiently diminishes outer-

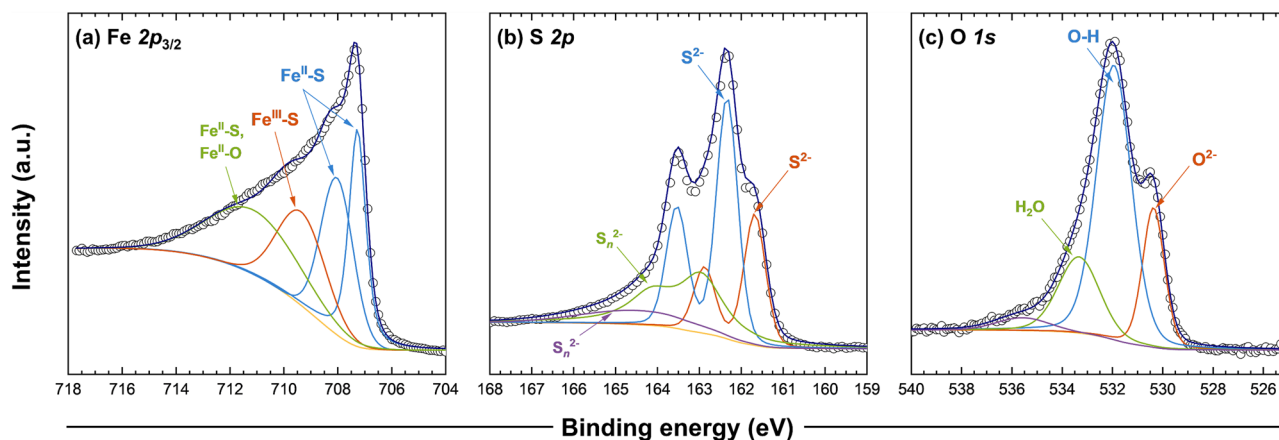


Fig. 2 | High resolution XPS spectra for the initial FeS, with calculated Fe/S of 0.76, as reported for mackinawite⁴⁸. Spectra shown are for Fe 2p_{3/2} (a), S 2p (b), and O 1s (c).

sphere adsorption, inner-sphere adsorption may still occur, as well as U(VI) entrapping during FeS particle aggregation⁵¹. Yet, this would also apply to the setup of previous work, and our work diverges from previous studies in that adsorption effects are limited.

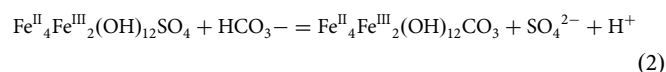
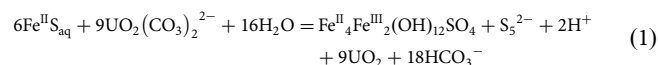
Mackinawite oxidation to green rust

Subsequent to U injection into the FeS slurry and during the first hours of the experiment, U was removed from solution following first-order kinetics (Fig. 3). The rates of U removal are very similar to previous work, with faster rates when no Ca is introduced to the system³⁶. Uraninite (UO₂) is commonly invoked as a solid U^{IV} end-product of U reduction by FeS, based on spectrometric methods^{26,34,36}, but it has only been observed by TEM imaging in two studies^{35,38}. Both our XPS and TEM results confirm the formation of UO₂ nanoparticles as the final U(IV) phase in our experiments (Fig. 4d-e), with *d*-spacings in agreement with the presence of uraninite nanoparticles^{25,52}. We also explored the products of FeS oxidation by U(VI). Our XPS results suggest that S species include mono- and polysulphides but exclude pyrite or other disulphides as end-products (Fig. 4b). This supports the formation of elemental S and polysulphide during the FeS oxidation reaction, again confirming results reported in both experimental^{34,35,38} and natural³⁷ studies.

The calculated Fe^{II}-S/Fe^{III}-S ratio of 0.28 on the Fe 2p_{3/2} XPS spectrum (Fig. 4a) suggests the presence of oxidized Fe^{III}-S species following reaction with U(VI). Such a ratio would correspond stoichiometrically to an intermediate phase between mackinawite and greigite. However, whilst greigite has been observed as a solid intermediate phase during the formation of pyrite^{33,39}, we found no TEM evidence for its presence in our experiments. Any Fe^{III}-S species could potentially be a consequence of alteration phases at the surface of mackinawite aggregates; but again, there was no TEM evidence supporting alteration patterns or oxidation products and the FeS aggregates persisted until the end of the reaction (Fig. 5a). Furthermore, while we cannot exclude inner-sphere complexation, outer-sphere adsorption through electrostatic interactions is not favoured in our experimental setup, with pH > pHPZC of mackinawite⁵³, and we presume that extensive U(VI) adsorption is hindered. Instead, we propose that FeS oxidation likely occurred via solubility-controlled dissolution.

At a pH of 8 and for millimolar S(-II) concentrations, the solubility of mackinawite is dominated by the formation of aqueous FeS_{aq} clusters, contrasting with the formation of Fe²⁺ under more acidic conditions⁵⁴. Therefore, in our experiment and in most FeS-rich seawater environments, reduction of uranium is likely to occur via the reaction with aqueous FeS_{aq}. Hence, we argue that Fe^{II}-S/Fe^{III}-S species are unlikely to form at the surface of solid FeS aggregates following U(VI) adsorption. Instead, our TEM results clearly document the presence of well-developed hexagonal structures (Fig. 5a-c), that were also Fe phases (as confirmed by EDX, Fig. S3). The

SAED point towards a mixed Fe^{II}/Fe^{III} hydroxide green rust, (Fig. 5d), and we therefore suggest that the mixed Fe^{II}-S/Fe^{III}-S XPS spectra may include, at least partly, some green rust component. Thermodynamic calculations (using PHREEQC/PhreePlot and the phreeqc.dat and wateq4f.dat database for uranium) further support the stability of green rust under our experimental Eh-pH conditions (Fig. S4). Because the starting Fe phase was FeS, it is reasonable to expect that the product consists of sulphate green rust (Fe₆(OH)₁₂SO₄), following the partial oxidation of both Fe and S, which is consistent with the presence of polysulphide (Eq. 1). However, the *d*-spacing measured by SAED (Fig. 5d) suggests carbonate green rust (Fe₆(OH)₁₂CO₃), which is smaller than the *d*-spacing of sulphate green rust⁵⁵. Our data confirm previously documented sulphate to carbonate green rust transformation by substitution⁵⁶ due to the high bicarbonate concentration in solution (Eq. 2). We also note that partial green rust oxidation during electron irradiation may have resulted in diminished *d*-spacings⁵⁷.



Large U isotope fractionation during green rust formation

We measured the isotope composition of U (i.e., the ²³⁸U/²³⁵U relative variation in permil compared to the starting composition, expressed as δ²³⁸U) of both dissolved U(VI) and solid U^{IV}O₂ (Supplementary methods 3 and 4). Our work extends on the findings in earlier reports^{26,36}, which primarily focussed on the isotopic evolution of the dissolved pool. Based on our experimental protocol, we can infer that U adsorption to the solid mackinawite nanoparticles was insignificant, because the negatively charged mackinawite surfaces at our experimental pH of our experiments will prevent substantial U adsorption⁵³. The subsequent formation of green rust as an oxidation product of the initial FeS may potentially induce U adsorption. However, at pH 8, the system is also close to the pHPZC of green rust⁵⁸, limiting the extent of U adsorption onto green rust surfaces. Similarly, the rapid transformation of sulphate to carbonate green rust would have negligible effects, as both species have a very similar pHPZC⁵⁵. Hence, and as supported by our spectroscopic and high resolution microscopic and analytical results, we conclude that any U that was associated with the solid particles in our experiments predominantly consisted of uraninite (Fig. 4d and e), and not surface-sorbed U. Yet, it is possible that an additional U isotope fractionation occurs upon reaction with neofomed green rust.

Table 1 | Elemental and isotope data for the entire set of experiments

Short term experiments <2 h														
Solids sample	time (h)	[Fe] ppm	[U] ppm	$\delta^{238}\text{U}$ (‰)	2σ (‰)	Solutions sample	time (h)	[Fe] ppm	[U] ppm	$\delta^{238}\text{U}$ (‰)	2σ (‰)	$\Delta^{238}\text{U U(VI)-U(IV)}$ (‰)	mass balance (‰)	2σ (‰)
FeS-1-S	0.00	56.0	0.0			FeS-1-D	0.00		16.0					
FeS-11-S	0.08	37.2	5.8	0.9	0.2	FeS-11-D	0.08	3.6	8.5	-1.0	0.2	-1.8	-0.2	0.3
FeS-12-S	0.08	38.2	5.9	0.7	0.2	FeS-12-D	0.08	3.9	9.7	-0.4	0.2	-1.1	0.0	0.3
FeS-13-S	0.25	37.7	6.3	0.7	0.1	FeS-13-D	0.25	3.1	7.2	-0.7	0.1	-1.5	-0.1	0.1
FeS-14-S	0.25	31.1	5.3	0.4	0.1	FeS-14-D	0.25	3.2	7.8	-0.5	0.1	-0.9	-0.1	0.1
FeS-15-S	0.50	39.4	7.1	0.6	0.1	FeS-15-D	0.50	3.8	8.2	-0.8	0.1	-1.4	-0.1	0.1
FeS-16-S	0.50	39.9	7.1	0.6	0.1	FeS-16-D	0.50	3.8	8.7	-0.7	0.1	-1.3	-0.1	0.1
FeS-17-S	1.17	38.2	7.4	0.7	0.1	FeS-17-D	1.17	3.7	8.2	-0.5	0.1	-1.2	0.0	0.1
Long term experiments >2 h														
Solids sample	time (h)	[Fe] ppm	[U] ppm	$\delta^{238}\text{U}$ (‰)	2σ (‰)	Solutions sample	time (h)	[Fe] ppm	[U] ppm	$\delta^{238}\text{U}$ (‰)	2σ (‰)	$\Delta^{238}\text{U U(VI)-U(IV)}$ (‰)	mass balance (‰)	2σ (‰)
FeS-1-S	0	56.0	0.0			FeS-1-D	0		16.0					
FeS-2-S	2.5	49.0	12.3	0.7	0.1	FeS-2-D	2.5	0.6	4.6	-1.4	0.1	-2.1	0.1	0.1
FeS-7-S	5	47.5	13.9	0.5	0.1	FeS-7-D	5	5.6	0.6	-2.9	0.1	-3.4	0.4	0.1
FeS-3-S	5	48.3	13.6	0.3	0.1	FeS-3-D	5	0.3	0.7	-2.8	0.1	-3.1	0.2	0.1
FeS-4-S	26	46.9	16.2	0.2	0.1	FeS-4-D	26	0.4	0.1	-0.7	0.1	-0.9	0.2	0.1
FeS-5-S	48	51.1	15.5	0.0	0.1	FeS-5-D	48	0.2	0.1	-0.8	0.1	-0.8	0.0	0.1
FeS-9-S	48	43.0	13.1	0.0	0.2	FeS-9-D	48	0.2	0.1	-0.6	0.2	-0.6	0.0	0.3
FeS-6-S	144	52.0	15.3	0.1	0.1	FeS-6-D	144	0.1	0.3	-0.8	0.1	-0.9	0.1	0.1
FeS-10-S	144	44.8	13.1	0.2	0.2	FeS-10-D	144	0.2	0.3	-0.5	0.2	-0.7	0.2	0.3

Also shown are mass balance calculations, which suggest full isotope recovery from both solids and solutions.

However, the effects of this mechanism would remain anecdotal, as there is no evidence for green rust oxidation products, and the main observed process is the oxidation of FeS to green rust.

Our results from the long-term experiments (Fig. 6a) showed a large U isotope fractionation favouring the incorporation of heavy U isotopes into the solid phase (UO₂), resulting in the formation of an isotopically light dissolved pool³⁶. The incorporation of heavy U isotopes in the solid phase contrasts with kinetic fractionation predictions, whereby solid products would incorporate the kinetically more labile, lighter isotopes. However, this is in agreement with nuclear field shift effects, where isotope fractionations are governed by changes in the nuclear charge density, as expected for heavier elements such as uranium^{27,28}. Yet, unlike in a previous study³⁶, our results indicate that the isotope fractionation between dissolved and solid U decreased with time. This suggests kinetic effects during the first hours of the experiment, prior to reaching a steady state between dissolved U(VI) and UO₂, where the isotope difference between U(VI) and U(IV)

($\Delta^{238}\text{U}_{\text{U(VI)-U(IV)}} \sim -0.8\text{‰}$) (Table 1, Fig. 6a). Indeed, initial $\Delta^{238}\text{U}_{\text{U(VI)-U(IV)}}$ reaches -3.4‰ during the first hours of experiment, when the U solution was injected immediately after FeS precipitation. This is in sharp contrast with the results in our short-term experiments (Table 1 and Fig. 6b), where FeS was first aged in its supernatant solution before initiating the reaction with U, and where initial $\Delta^{238}\text{U}_{\text{U(VI)-U(IV)}}$ remained closer to the final $\Delta^{238}\text{U}_{\text{U(VI)-U(IV)}}$ of -1.2‰ (Table 1). Previous isotope⁵⁶ and small-angle X-ray scattering⁵⁷ studies have identified aggregation growth as the mechanism leading to mackinawite assembly in the earliest steps of FeS precipitation. We therefore suggest that the large apparent isotope fractionation in the long-term experiments are the result of rapid FeS nanoparticle growth via oriented aggregation mechanism^{51,59}, which may record the highest expression of U isotope fractionations. During subsequent isotope exchange, the system quickly reaches a steady state, which resembles the short-term experiment steady state ($\Delta^{238}\text{U}_{\text{U(VI)-U(IV)}} \sim -1\text{‰}$). In both cases, the evolution of the isotope composition scales logarithmically with the removal of U(VI)_{aq} from solution (Fig. 7), confirming earlier studies^{26,36}, with a substantial shift when data include initial, short term particle growth, or when data solely reflect longer-term isotope fractionations.

Our results, pointing towards a large, apparent isotope fractionation recorded as steady state sharply contrasts with previous studies in the absence of calcium^{26,36}. We envisage that this discrepancy is due to (1) the minimisation of adsorption effects, which may fractionate U isotopes in opposite direction to reduction effects⁵⁰, in turn diminishing the extent of apparent fractionation; (2) the fundamentally different mechanism for FeS dissolution at higher pH, involving FeS_{aq} clusters over Fe²⁺, and the partial oxidation of FeS_{aq} to green rust. Hence, we propose that in most FeS-rich seawater environments with pH >7, the reduction of uranium by FeS likely occurs via the formation of FeS_{aq} and green rust phases, and that this reaction is indeed accompanied by a large U isotope fractionation, which concentrates the heavier isotopes in the reduced (solid) phase, with U isotope compositions approximately 1‰ more positive than the residual solution.

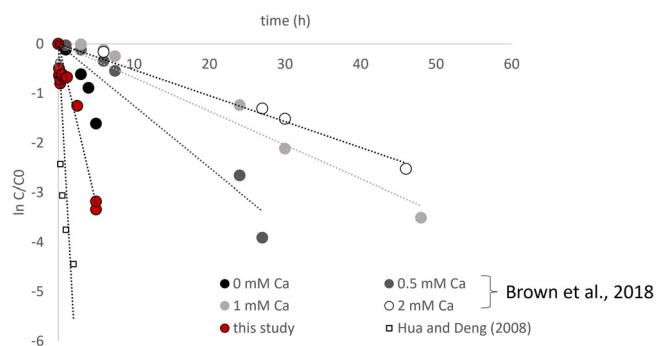


Fig. 3 | Linearized dissolved U concentrations through time, during U^{VI} removal from solution. Our study compares well to previous work^{34,36}, suggesting 1st order kinetics for the rate of U removal with no Ca present in solution.

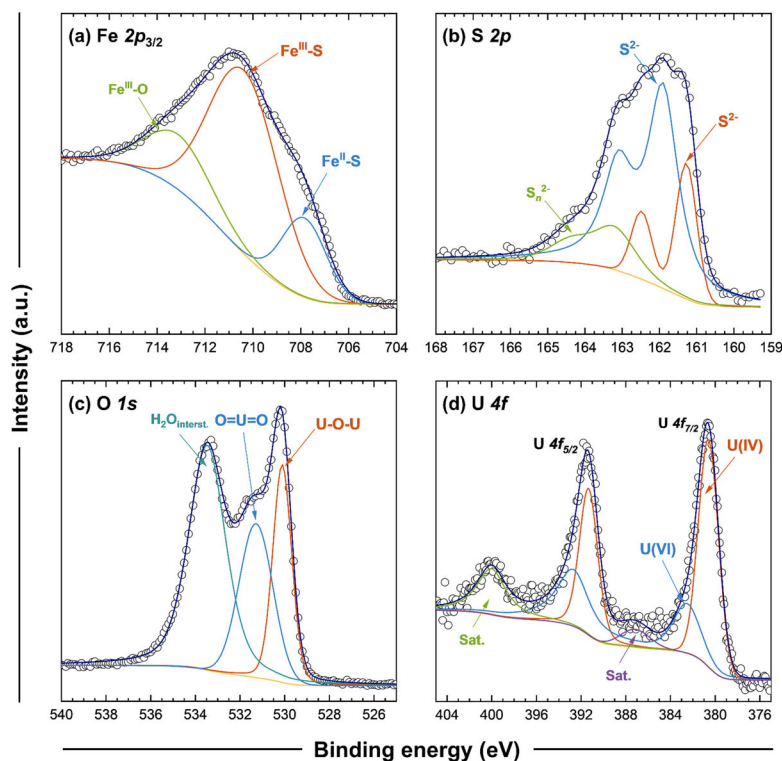
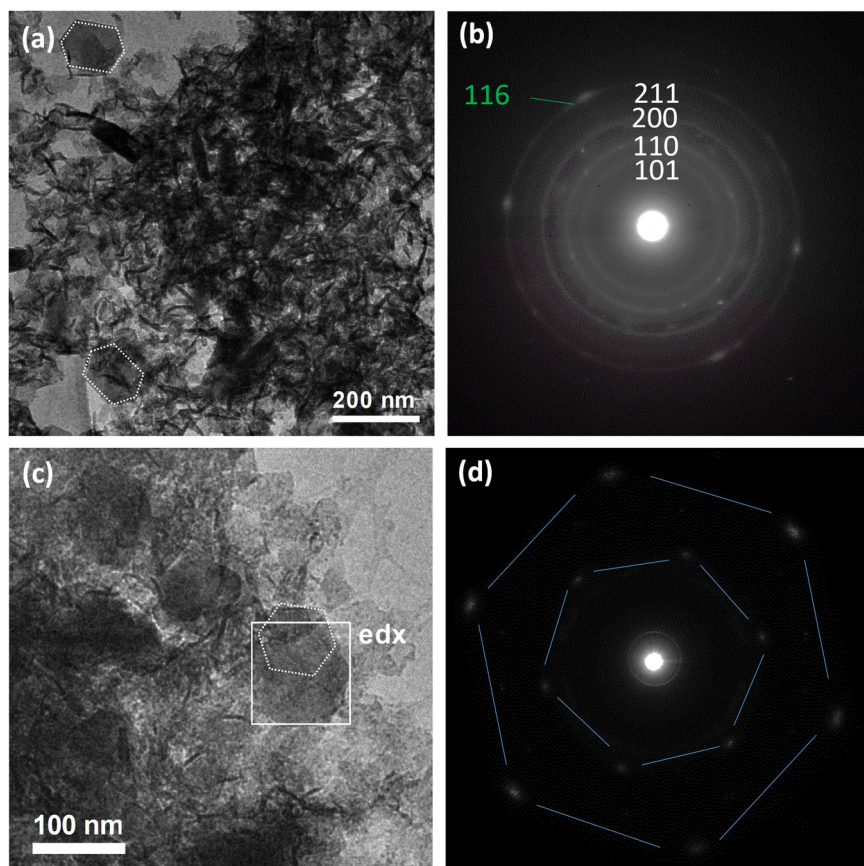


Fig. 4 | High resolution XPS spectra of the mineralogical products after one day of experiment. Spectra are shown for Fe 2p_{3/2} (a), S 2p (b), O 1s (c) and U 4f (d), and TEM image with FFT patterns of nanocrystalline uraninite (e).

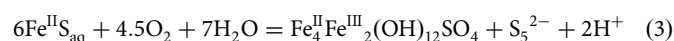
Fig. 5 | TEM data supporting green rust production. (a) TEM image of FeS aggregates and green rust hexagons (highlighted by dotted white lines) after one day of experiment, as confirmed by the SAED peaks in (b). (c) Visible hexagonal structures (highlighted by dotted white lines) where an EDX analyses was carried out (supplementary information Fig. S3), and (d) typical green rust hexagonal patterns identified by SAED, with the outer ring corresponding to the 116 lattice plane of the carbonated species (in green)⁵⁵.



Discussion: Implications for Precambrian redox transitions. The highly dynamic nature of ocean redox chemistry in the Precambrian highlights the significance of redox transitional zones for the reconstruction of ancient biogeochemical cycles. In modern environments, the mineralogy of such transitions can be explored through the study of redoxclines, or more generally at the interface between different redox settings. For instance, in modern ferruginous analogues, the redox interface between shallow, oxygenated waters and anoxic, Fe-containing deeper waters, is characterized by the precipitation of ferrihydrite and its partial reduction to green rust^{23,24,60}. Magnetite also plays a major role as an end-product of the rapid transformation of metastable green rust species^{24,58,61}, or potentially as a primary precipitate at the oxic-ferruginous interface⁶².

At the redoxcline of euxinic environments, the release of Fe(II) upon reduction of Fe (oxyhydr)oxides by H₂S may promote the formation of an anoxic and non-sulphidic layer. An eloquent example for such non-sulphidic interface above euxinic deeper waters is the Black Sea, with several meters of Mn-rich water between the strictly oxic and strictly euxinic water masses⁶³, but thinner anoxic and ferruginous interfaces have also been reported in euxinic lakes⁶⁴. Modern oxygenated ferro-euxinic springs, considered analogous to ancient anoxic-oxic transitions, have reported elemental sulphur and green rust as dominant mineral phases³⁷. Such environments may be characteristic of suboxic settings, where low levels of oxygen dominate, or at the interfaces between strictly oxic and strictly anoxic conditions. Our study supports the natural observations, and further hints at the fact that the partial oxidation of FeS, a preponderant metastable mineral in strictly euxinic systems⁶⁵, indeed leads to the formation of green rust. We showed that 9 moles of U(VI) are sufficient to partially oxidise 6 moles of FeS into 1 mole of green rust and polysulphide (Eq. 1). We note that polysulphide may further react with FeS_{aq} to nucleate pyrite under euxinic conditions^{65,66}, as a competing mechanism for FeS partial oxidation. Although we did not observe pyrite formation in our experiments, this could

be kinetically hindered, and potential U isotope fractionations during U(VI) reduction by pyrite have never been determined. Assuming oxygen is the only oxidant source in the system (as opposed to uranium), the reaction would be equivalent to the oxidation of 6 moles of FeS by 4.5 moles of oxygen (Eq. 3). From our experimental set up, where we started with ~70 μM U(VI), we infer that oxygen concentrations of 35 μM are sufficient to drive the partial oxidation of FeS into green rust and polysulphide.



In such environments, U isotopes may fractionate substantially during the partial oxidation to green rust, with the preferential incorporation of ²³⁸U into uraninite. Therefore, our study implies that chemocline fluctuations between strictly euxinic (containing FeS suspensions) and ‘suboxic’ conditions along Proterozoic continental margins⁶⁷ are likely to have led to the formation of green rust minerals in the water column, and to the deposition of sediments being dominantly enriched in heavy U isotopes. An abiotic $\Delta^{238}\text{U}_{\text{sediment-water}}$ of ~1‰ is substantially larger than the typical level of $\delta^{238}\text{U}_{\text{sediment-water}}$ observed in modern euxinic basins (~0.5‰)^{9,10,27}. While U reduction driven by bacterial sulphate-reduction within sediments is expected to dominate U uptake under strongly euxinic conditions, it may be diminished under less extreme, transitional redox settings⁷⁷. Therefore, abiotic U reduction during partial FeS oxidation to green rust may have played a prominent role for authigenic U enrichments within zones of transitional redox conditions in the Precambrian oceans. This reinforces previous views^{34,61} that green rusts are key minerals for the reconstruction of Precambrian environments, due to their ubiquity in ferruginous, ‘suboxic’ and transitional redox settings. Such sedimentary systems should be detected by substantial $\Delta^{238}\text{U}_{\text{sediment-water}}$ (~1‰) and a high authigenic $\delta^{238}\text{U}$ component in anoxic sediments. High authigenic $\delta^{238}\text{U}$ compared to seawater has been observed in sediments from the chemocline of the Black Sea⁶⁸, as well as in Mediterranean sapropels characterised by weakly or temporal euxinic

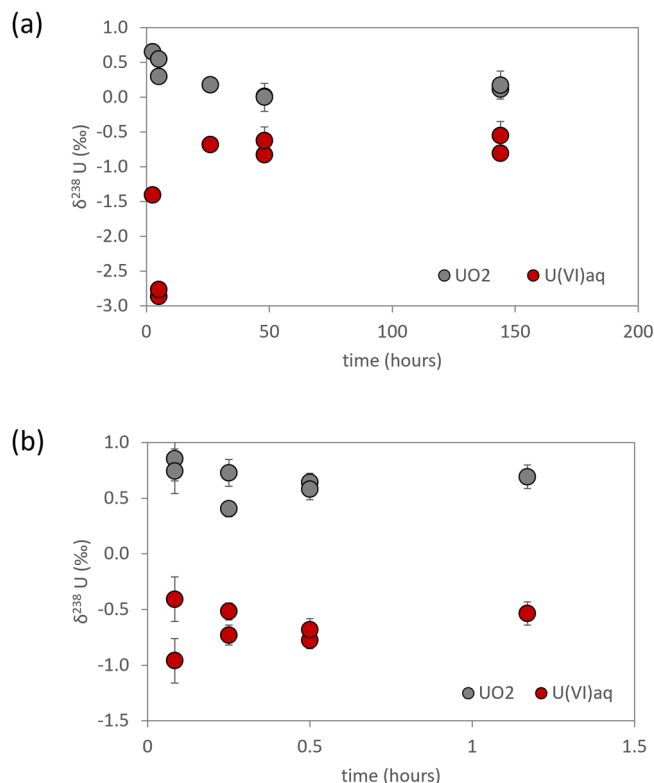


Fig. 6 | Isotopic evolution of dissolved U^{VI} and solid UO_2 through the experiment. Heavy U isotopes are preferentially incorporated into uraninite, as predicted for nuclear field shift effects. (a) Long-term experiments, where U injection was immediately following FeS precipitation; (b) short-term experiments, where U injection was done only after 1 h of aging the precipitated FeS in its supernatant.

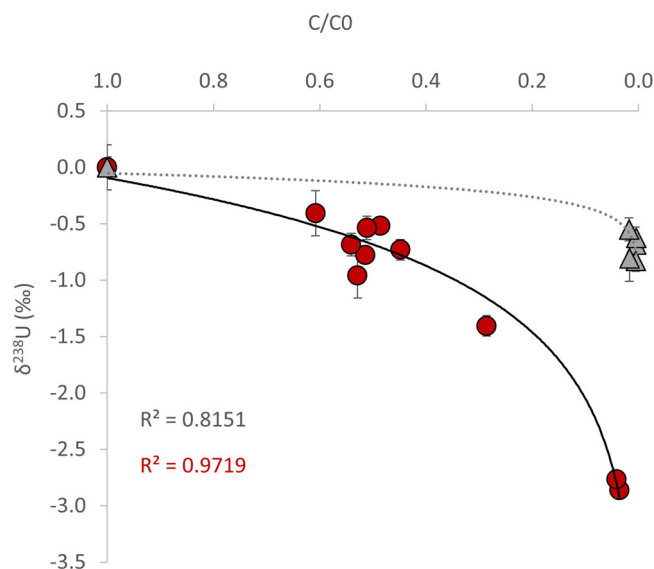


Fig. 7 | Evolution of $\delta^{238}U$ in solution as a function of U remaining in the solution, for the experimental dataset <48 h in red, and >48 h in grey. C stands for U concentration at any given time, and C_0 stands for initial U concentrations. The data best fit with a logarithmic trend, with $R^2 = 0.97$ for <48 h experiments, and $R^2 = 0.82$ for >48 h experiments. The substantial shift between both datasets is best explained by initial particle growth effects (in red) versus longer term isotope fractionations at steady state (in grey).

conditions^{68,69} and in a range of Paleoproterozoic to early Phanerozoic sediments^{1,70–72}. While there are different ways to explain higher $\delta^{238}U$ than observed in modern euxinic sediments^{3,68,73}, we suggest that abiotic U reduction during partial FeS oxidation to green rust may have contributed a substantial part of authigenic U enrichments in such sediments.

Data availability

All data are included in present paper.

Received: 26 April 2024; Accepted: 31 January 2025;

Published online: 08 February 2025

References

- Asael, D. et al. Coupled molybdenum, iron and uranium stable isotopes as oceanic paleoredox proxies during the Paleoproterozoic Shunga Event. *Chem. Geol.* **362**, 193–210 (2013).
- Romaniello, S. J., Herrmann, A. D. & Anbar, A. D. Uranium concentrations and 238 U/235 U isotope ratios in modern carbonates from the Bahamas: Assessing a novel paleoredox proxy. *Chem. Geol.* **362**, 305–316 (2013).
- Andersen, M. et al. A modern framework for the interpretation of 238 U/235 U in studies of ancient ocean redox. *Earth Planet. Sci. Lett.* **400**, 184–194 (2014).
- Brennecke, G. A., Herrmann, A. D., Algeo, T. J. & Anbar, A. D. Rapid expansion of oceanic anoxia immediately before the end-Permian mass extinction. *Proc. Natl. Acad. Sci.* **108**, 17631–17634 (2011).
- Brennecke, G. A., Wasylenki, L. E., Bargar, J. R., Weyer, S. & Anbar, A. D. Uranium isotope fractionation during adsorption to Mn-oxyhydroxides. *Environ. Sci. Technol.* **45**, 1370–1375 (2011).
- Kendall, B., Brennecke, G. A., Weyer, S. & Anbar, A. D. Uranium isotope fractionation suggests oxidative uranium mobilization at 2.50 Ga. *Chem. Geol.* **362**, 105–114 (2013).
- Chen, X. et al. Diagenetic effects on uranium isotope fractionation in carbonate sediments from the Bahamas. *Geochimica et. Cosmochimica Acta* **237**, 294–311 (2018).
- Chen, X., Romaniello, S. J., Herrmann, A. D., Wasylenki, L. E. & Anbar, A. D. Uranium Isotope Fractionation During Coprecipitation with Aragonite and Calcite. *Geochimica et. Cosmochimica Acta*, (2016).
- Weyer, S. et al. Natural fractionation of 238U/235U. *Geochimica et. Cosmochimica Acta* **72**, 345–359 (2008).
- Bura-Nakić, E. et al. Coupled Mo-U abundances and isotopes in a small marine euxinic basin: Constraints on processes in euxinic basins. *Geochimica et. Cosmochimica Acta* **222**, 212–229 (2018).
- Planavsky, N. J. et al. Widespread iron-rich conditions in the mid-Proterozoic ocean. *Nature* **477**, 448–451 (2011).
- Poulton, S. W. & Canfield, D. E. Ferruginous Conditions: A Dominant Feature of the Ocean through Earth’s History. *Elements* **7**, 107–112 (2011).
- Poulton, S. W., Fralick, P. W. & Canfield, D. E. Spatial variability in oceanic redox structure 1.8 billion years ago. *Nat. Geosci.* **3**, 486–490 (2010).
- Guilbaud, R., Poulton, S. W., Butterfield, N. J., Zhu, M. & Shields-Zhou, G. A. A global transition to ferruginous conditions in the early Neoproterozoic oceans. *Nat. Geosci.* **8**, 466–470 (2015).
- Sperling, E. A. et al. Statistical analysis of iron geochemical data suggests limited late Proterozoic oxygenation. *Nature* **523**, 451–454 (2015).
- Johnston, D. T. et al. An emerging picture of Neoproterozoic ocean chemistry: Insights from the Chuar Group, Grand Canyon, USA. *Earth Planet. Sci. Lett.* **290**, 64–73 (2010).
- Canfield, D. E. et al. Ferruginous Conditions Dominated Later Neoproterozoic Deep-Water Chemistry. *Science* **321**, 949–952 (2008).

18. Wood, R. et al. Dynamic redox conditions control late Ediacaran metazoan ecosystems in the Nama Group, Namibia. *Precambrian Res.* **261**, 252–271 (2015).
19. Tostevin, R. et al. Low-oxygen waters limited habitable space for early animals. *Nat. Commun.* **7**, 12818 (2016).
20. Hammarlund, E. U. et al. Early Cambrian oxygen minimum zone-like conditions at Chengjiang. *Earth & Planetary Science Letters*, (2017).
21. Guilbaud, R. et al. Oxygen minimum zones in the early Cambrian ocean. *Geochemical Perspect. Lett.* **6**, 33–38 (2018).
22. Jin, C. et al. A highly redox-heterogeneous ocean in South China during the early Cambrian (~529–514 Ma): Implications for biota-environment co-evolution. *Earth Planet. Sci. Lett.* **441**, 38–51 (2016).
23. Konhauser, K. O. et al. Decoupling photochemical Fe (II) oxidation from shallow-water BIF deposition. *Earth Planet. Sci. Lett.* **258**, 87–100 (2007).
24. Zegeye, A. et al. Green rust formation controls nutrient availability in a ferruginous water column. *Geology* **40**, 599–602 (2012).
25. O'Loughlin, E. J., Kelly, S. D., Cook, R. E., Csencsits, R. & Kemner, K. M. Reduction of Uranium(VI) by Mixed Iron(II)/Iron(III) Hydroxide (Green Rust): Formation of UO₂ Nanoparticles. *Environ. Sci. Technol.* **37**, 721–727 (2003).
26. Stylo, M. et al. Uranium isotopes fingerprint biotic reduction. *Proc. Natl. Acad. Sci. USA* **112**, 5619 (2015).
27. Andersen, M. B., Stirling, C. H. & Weyer, S. Uranium isotope fractionation. *Rev. Mineral. Geochem.* **82**, 799–850 (2017).
28. Schauble, E. A. Role of nuclear volume in driving equilibrium stable isotope fractionation of mercury, thallium, and other very heavy elements. *Geochimica et. Cosmochimica Acta* **71**, 2170–2189 (2007).
29. Cole, D. B. et al. Uranium isotope fractionation in non-sulfidic anoxic settings and the global uranium isotope mass balance. *Glob. Biogeochemical Cycles* **34**, e2020GB006649 (2020).
30. Lovley, D. R., Roden, E. E., Phillips, E. J. P. & Woodward, J. C. Enzymatic iron and uranium reduction by sulfate-reducing bacteria. *Mar. Geol.* **113**, 41–53 (1993).
31. Rickard, D. & Luther, G. W. Kinetics of pyrite formation by the H₂S oxidation of iron (II) monosulfide in aqueous solutions between 25 8C and 125 8C: the mechanism. *Geochim. Cosmochim. Acta* **61**, 135–147 (1997).
32. Rickard, D. Kinetics of FeS precipitation: Part 1. Competing reaction mechanisms. *Geochim. Cosmochim. Acta* **59**, 4367–4379 (1995).
33. Benning, L. G., Wilkin, R. T. & Barnes, H. L. Reaction pathways in the Fe–S system below 1008C. *Chem. Geol.* **167**, 25–51 (2000).
34. Hua, B. & Deng, B. Reductive immobilization of uranium (VI) by amorphous iron sulfide. *Environ. Sci. Technol.* **42**, 8703–8708 (2008).
35. Veeramani, H. et al. Abiotic reductive immobilization of U (VI) by biogenic mackinawite. *Environ. Sci. Technol.* **47**, 2361–2369 (2013).
36. Brown, S. T., Basu, A., Ding, X., Christensen, J. N. & DePaolo, D. J. Uranium isotope fractionation by abiotic reductive precipitation. *Proceedings of the National Academy of Sciences* 201805234 (2018).
37. Koeksoy, E. et al. Formation of green rust and elemental sulfur in an analogue for oxygenated ferro-euxinic transition zones of Precambrian oceans. *Geology* **47**, 211–214 (2019).
38. Hyun, S. P., Davis, J. A., Sun, K. & Hayes, K. F. Uranium(VI) Reduction by Iron(II) Monosulfide Mackinawite. *Environ. Sci. Technol.* **46**, 3369–3376 (2012).
39. Hunger, S. & Benning, L. G. Greigite: a true intermediate on the polysulfide pathway to pyrite. *Geochemical Trans.* **8**, 1 (2007).
40. Kennedy, T. & Sturman, B. The oxidation of iron (II) sulphide. *J. Therm. Anal. Calorim.* **8**, 329–337 (1975).
41. Jeong, H. Y., Han, Y.-S., Park, S. W. & Hayes, K. F. Aerobic oxidation of mackinawite (FeS) and its environmental implication for arsenic mobilization. *Geochimica et. Cosmochimica Acta* **74**, 3182–3198 (2010).
42. Schippers, A. & Jørgensen, B. Oxidation of pyrite and iron sulfide by manganese dioxide in marine sediments. *Geochimica et. Cosmochimica Acta* **65**, 915–922 (2001).
43. Chiriță, P. Iron monosulfide (FeS) oxidation by dissolved oxygen: characteristics of the product layer. *Surf. Interface Anal.* **41**, 405–411 (2009).
44. Park, M., Park, J., Kang, J., Han, Y.-S. & Jeong, H. Y. Removal of hexavalent chromium using mackinawite (FeS)-coated sand. *J. Hazard. Mater.* **360**, 17–23 (2018).
45. Guilbaud, R., Butler, I. B., Ellam, R. M., Rickard, D. & Oldroyd, A. Experimental determination of the equilibrium Fe isotope fractionation between and FeS m (mackinawite) at 25 and 2 °C. *Geochimica et. Cosmochimica Acta* **75**, 2721–2734 (2011).
46. Jeong, H. Y., Lee, J. H. & Hayes, K. F. Characterization of synthetic nanocrystalline mackinawite: Crystal structure, particle size, and specific surface area. *Geochimica et. Cosmochimica Acta* **72**, 493–505 (2008).
47. Ohfui, H. & Rickard, D. High resolution transmission electron microscopic study of synthetic nanocrystalline mackinawite. *Earth Planet. Sci. Lett.* **241**, 227 (2006).
48. Matamoros-Veloza, A. et al. A highly reactive precursor in the iron sulfide system. *Nat. Commun.* **9**, 3125 (2018).
49. Wolthers, M., Charlet, L., van Der Linde, P. R., Rickard, D. & van Der Weijden, C. H. Surface chemistry of disordered mackinawite (FeS). *Geochimica et. Cosmochimica Acta* **69**, 3469–3481 (2005).
50. Jemison, N. E., Johnson, T. M., Shiel, A. E. & Lundstrom, C. Uranium isotopic fractionation induced by U (VI) adsorption onto common aquifer minerals. *Environ. Sci. Technol.* **50**, 12232–12240 (2016).
51. Guilbaud, R., Butler, I. B., Ellam, R. M. & Rickard, D. Fe isotope exchange between Fe (II)_{aq} and nanoparticulate mackinawite (FeS_m) during nanoparticle growth. *Earth Planet. Sci. Lett.* **300**, 174–183 (2010).
52. Rundle, R., Baenziger, N., Wilson, A. & McDonald, R. The structures of the carbides, nitrides and oxides of uranium¹. *J. Am. Chem. Soc.* **70**, 99–105 (1948).
53. Wolthers, M., van der Gaast, S. J., Charlet, L. & Rickard, D. A surface and structural model describing the environmental reactivity of disordered mackinawite. *Am. Mineral.* **88**, 2007–2015 (2005).
54. Rickard, D. The solubility of FeS. *Geochimica et. Cosmochimica Acta* **70**, 5779–5789 (2006).
55. Usman, M. et al. Magnetite and green rust: synthesis, properties, and environmental applications of mixed-valent iron minerals. *Chem. Rev.* **118**, 3251–3304 (2018).
56. Perez, J. P. H. et al. Arsenic removal from natural groundwater using 'green rust': Solid phase stability and contaminant fate. *J. Hazard. Mater.* **401**, 123327 (2021).
57. Freeman, H. M., Perez, J. P. H., Hondow, N., Benning, L. G. & Brown, A. P. Beam-induced oxidation of mixed-valent Fe (oxyhydr)oxides (green rust) monitored by STEM-EELS. *Micron* **122**, 46–52 (2019).
58. Guilbaud, R., White, M. L. & Poulton, S. W. Surface charge and growth of sulphate and carbonate green rust in aqueous media. *Geochimica et. Cosmochimica Acta* **108**, 141–153 (2013).
59. Matamoros-Veloza, A., Stawski, T. M. & Benning, L. G. Nanoparticle Assembly Leads to Mackinawite Formation. *Cryst. Growth Des.* **18**, 6757–6764 (2018).
60. Cosmidis, J. et al. Biomineralization of iron-phosphates in the water column of Lake Pavin (Massif Central, France). *Geochimica et. Cosmochimica Acta* **126**, 78–96 (2014).
61. Halevy, I., Alesker, M., Schuster, E., Popovitz-Biro, R. & Feldman, Y. A key role for green rust in the Precambrian oceans and the genesis of iron formations. *Nat. Geosci.* **10**, 135–139 (2017).
62. Li, Y.-L., Konhauser, K. O. & Zhai, M. The formation of magnetite in the early Archean oceans. *Earth Planet. Sci. Lett.* **466**, 103–114 (2017).
63. Murray, J. W. et al. Unexpected changes in the oxic/anoxic interface in the Black Sea. *Nature* **338**, 411–413 (1989).
64. Xiong, Y. et al. Phosphorus cycling in Lake Cadagno, Switzerland: A low sulfate euxinic ocean analogue. *Geochimica et. Cosmochimica Acta* **251**, 116–135 (2019).

65. Rickard, D. & Luther, G. W. Chemistry of Iron Sulfides. *Chem. Rev.* **107**, 514–562 (2007).
66. Luther, G. W. Pyrite synthesis via polysulfide compounds. *Geochim. Cosmochim. Acta* **55**, 2839–2849 (1991).
67. Lyons, T. W., Reinhard, C. T. & Planavsky, N. J. The rise of oxygen in Earth's early ocean and atmosphere. *Nature* **506**, 307–315 (2014).
68. Clarkson, M. O. et al. Environmental controls on very high $\delta^{238}\text{U}$ values in reducing sediments: Implications for Neoproterozoic seawater records. *Earth-Sci. Rev.* **237**, 104306 (2023).
69. Andersen, M. B., Matthews, A., Bar-Matthews, M. & Vance, D. Rapid onset of ocean anoxia shown by high U and low Mo isotope compositions of sapropel S1. *Geochemical Perspect. Lett.* **15**, 10–14 (2020).
70. Dang, D. et al. Authigenic uranium isotopes of late Proterozoic black shale. *Chem. Geol.* **588**, 120644 (2022).
71. Kendall, B. et al. Uranium and molybdenum isotope evidence for an episode of widespread ocean oxygenation during the late Ediacaran Period. *Geochimica et. Cosmochimica Acta* **156**, 173–193 (2015).
72. Cheng, K., Elrick, M. & Romaniello, S. J. Early Mississippian ocean anoxia triggered organic carbon burial and late Paleozoic cooling: Evidence from uranium isotopes recorded in marine limestone. *Geology* **48**, 363–367 (2020).
73. Lau, K. V., Lyons, T. W. & Maher, K. Uranium reduction and isotopic fractionation in reducing sediments: Insights from reactive transport modeling. *Geochimica et. Cosmochimica Acta* **287**, 65–92 (2020).

Acknowledgements

This work was funded by a Helmholtz Centre/GFZ short-term stay, a Royal Society Research Grant (RSG\R1\180326) and ANR grant agreement ANR-21-CE49-0007-01 to RG, and a Royal Society Research Grant (RSG\R1\160890) to MA. JPHP and LGB acknowledge the funding from the European Union's Horizon 2020 Marie Skłodowska-Curie Innovative Training Network METAL-AID (grant no. 675219), and the Helmholtz Recruiting Initiative (award no. I-044-16-01) awarded to LGB. JPHP is in part funded by the GFZ Discovery Fellowship (grant no. P-032-45-002). ICP-OES analyses were carried out at the Helmholtz Laboratory for the Geochemistry of the Earth Surface (HELGES) at GFZ Potsdam. XPS data were collected at the BAM Federal Institute for Materials Research and Testing, and the authors thank Dr. Jörg Radnik for the help. TEM analyses were carried out at the German Research Centre for Geosciences in the Potsdam Imaging and Spectral Analyses (PISA) facility that is partly funded by the European Regional Development Fund and the State of Brandenburg. We thank 3 anonymous reviewers for their constructive comments.

Author contributions

RG designed and performed the experiments. MBA analysed the uranium isotope composition of the samples. HMF performed the TEM analysis with RG and interpreted the TEM data with RG and LGB. JPHP performed the XPS analysis, and interpreted the XPS data with RG and LGB. DU performed the elemental analysis. The manuscript was initially written by RG, with significant contribution from MBA, HMF, JPHP, DU and LGB.

Competing interests

The authors declare no competing interests.

Additional information

Supplementary information The online version contains supplementary material available at <https://doi.org/10.1038/s43247-025-02088-5>.

Correspondence and requests for materials should be addressed to Romain Guillaud.

Peer review information *Communications Earth & Environment* thanks Abu Saeed Baidya and the other, anonymous, reviewer(s) for their contribution to the peer review of this work. Primary Handling Editors: Carolina Ortiz Guerrero. A peer review file is available.

Reprints and permissions information is available at <http://www.nature.com/reprints>

Publisher's note Springer Nature remains neutral with regard to jurisdictional claims in published maps and institutional affiliations.

Open Access This article is licensed under a Creative Commons Attribution 4.0 International License, which permits use, sharing, adaptation, distribution and reproduction in any medium or format, as long as you give appropriate credit to the original author(s) and the source, provide a link to the Creative Commons licence, and indicate if changes were made. The images or other third party material in this article are included in the article's Creative Commons licence, unless indicated otherwise in a credit line to the material. If material is not included in the article's Creative Commons licence and your intended use is not permitted by statutory regulation or exceeds the permitted use, you will need to obtain permission directly from the copyright holder. To view a copy of this licence, visit <http://creativecommons.org/licenses/by/4.0/>.

© The Author(s) 2025